

ARTICLE

Open Access

# Conversion of p–n conduction type by spinodal decomposition in Zn-Sb-Bi phase-change alloys

Guoxiang Wang<sup>1,2,3</sup>, Haizhou Shi<sup>1,3</sup>, Andriy Lotnyk<sup>2</sup>, Daotian Shi<sup>1,3</sup> and Rongping Wang<sup>1,3</sup>

## Abstract

Phase-change films with multiple resistance levels are promising for increasing the storage density in phase-change memory technology. Diffusion-dominated Zn<sub>2</sub>Sb<sub>3</sub> films undergo transitions across three states, from high through intermediate to low resistance, upon annealing. The properties of the Zn<sub>2</sub>Sb<sub>3</sub> material can be further optimized by doping with Bi. Based on scanning transmission electron microscopy combined with electrical transport measurements, at a particular Bi concentration, the conduction of Zn-Sb-Bi compounds changes from p- to n-type, originating from spinodal decomposition. Simultaneously, the change in the temperature coefficient of resistivity shows a metal-to-insulator transition. Further analysis of microstructure characteristics reveals that the distribution of the Bi-Sb phase may be the origin of the driving force for the p–n conduction and metal-to-insulator transitions and therefore may provide us with another way to improve multilevel data storage. Moreover, the Bi doping promotes the thermoelectric properties of the studied alloys, leading to higher values of the power factor compared to known reported structures. The present study sheds valuable light on the spinodal decomposition process caused by Bi doping, which can also occur in a wide variety of chalcogenide-based phase-change materials. In addition, the study provides a new strategy for realizing novel p–n heterostructures for multilevel data storage and thermoelectric applications.

## Introduction

With the rapid development of mobile electronic devices, artificial intelligence, and cloud computing, the amount of digital data in the global world is doubling every 2 years. As a result, the volume of digital data will reach 175 zettabytes in 2025<sup>1</sup>. Currently, storage devices, such as hard disc drives or NAND flash memories, are widely employed in data centers to store digital data. However, the huge performance and density gaps between the working memory (DRAM) and the storage devices in the memory hierarchy lead to failure in meeting the massive data storage requirements. Phase-change memory (PCM) is an emerging high-density nonvolatile memory technology that might replace the current Si-based flash memory

in the future<sup>2</sup>. PCM is based on the reversible switching between the amorphous and crystalline states of a phase-change material induced by either a laser or an electrical pulse, and such reversible switching is always associated with a large change in the resistance and optical reflectivity<sup>3</sup>. Recently, the design of novel structures in PCM suitable for multilevel storage operations has been developed. Such structures can save the information as multiple intermediate resistance levels between the high-resistance, entirely amorphous phase and the low resistance, entirely crystalline state, thus realizing storage of multiple bits within one cell<sup>4–6</sup>. For example, Ge<sub>2</sub>Sb<sub>2</sub>Te<sub>5</sub> (GST) alloy can be in three states, e.g., the amorphous, cubic and trigonal crystalline phases<sup>7</sup>. Therefore, multilevel data storage technology has been realized in GST with different resistance states within one cell.

However, the poor amorphous thermal stability of GST results in resistance drift of the phase. This factor has a negative effect on data storage in multiple intermediate memory levels, leading to memory failure<sup>8</sup>. Therefore,

Correspondence: Guoxiang Wang (wangguoxiang@nbu.edu.cn)

<sup>1</sup>Laboratory of Infrared Materials and Devices, The Research Institute of Advanced Technologies, Ningbo University, Ningbo, Zhejiang 315211, China

<sup>2</sup>Leibniz Institute of Surface Engineering (IOM), Permoserstr. 15, D-04318 Leipzig, Germany

Full list of author information is available at the end of the article

© The Author(s) 2020



**Open Access** This article is licensed under a Creative Commons Attribution 4.0 International License, which permits use, sharing, adaptation, distribution and reproduction in any medium or format, as long as you give appropriate credit to the original author(s) and the source, provide a link to the Creative Commons license, and indicate if changes were made. The images or other third party material in this article are included in the article's Creative Commons license, unless indicated otherwise in a credit line to the material. If material is not included in the article's Creative Commons license and your intended use is not permitted by statutory regulation or exceeds the permitted use, you will need to obtain permission directly from the copyright holder. To view a copy of this license, visit <http://creativecommons.org/licenses/by/4.0/>.

although multilevel storage is an effective approach to increase the data storage capacity, it is still challenging to prepare phase-change films with desired properties.

Te-free Sb-based alloys, such as Zn-Sb<sup>9</sup>, Ga-Sb<sup>10</sup>, and Er-Sb<sup>11</sup>, show strong feasibility as phase-change materials for PCM owing to the simplicity of their composition and explosive crystallization behavior of Sb<sup>9–11</sup>. Among them, Zn-Sb has recently attracted special interest due to its two-step crystallization process with metastable and stable ZnSb phases. In particular, ZnSb films have a higher crystallization temperature ( $\sim 257^\circ\text{C}$ ), a larger crystallization activation energy ( $\sim 5.63\text{ eV}$ ), better 10-year data retention ( $\sim 201^\circ\text{C}$ ) and a lower melting temperature ( $\sim 500^\circ\text{C}$ ) than the other alloys<sup>9</sup>. Despite its excellent thermal properties, the intrinsic conduction type of ZnSb is p-type, and the absence of n-type conduction limits its electronic applications<sup>12</sup>. Therefore, it is essential to explore methods for tuning the conduction type to expand the use of Zn-Sb in phase-change memory and thermoelectric devices.

It is well known that Bi metal has been used to obtain carrier-type conversion in chalcogenide alloys, where the carrier type is sensitive to the concentration of the Bi dopant. For example, Hughes et al.<sup>13</sup> reported n-type doping of chalcogenide glasses by ion implantation of 0.6 at% Bi into GaLaSO amorphous films, demonstrating rectification and a photocurrent in a Bi-implanted GaLaSO device. Similarly, Park et al.<sup>14</sup> found that the carrier type changed from the native p-type in GST to the n-type in GST doped with more than  $\sim 10$  at% Bi. It is suggested that Bi unpins the Fermi level and thus changes the conduction from p- to n-type<sup>15</sup>. There is also evidence that the effect of Bi doping is associated with coordination topological defect formation in the form of under- and/or overcoordinated atoms, such as positively ( $\text{Bi}^{3+}$  or  $\text{Bi}^{4+}$ ) and/or negatively ( $\text{Bi}^{2-}$  or  $\text{Bi}^{6-}$ ) charged defect centers<sup>16</sup>. Similar p- to n-type transitions have also been observed in arsenic and germanium selenide alloys at critical dopant concentrations. This is ascribed to the n-type  $\text{BiSe}_{3/2}$ -rich regions occurring as partially ordered nanoribbon sheets<sup>17</sup> or to the percolation transition threshold being reached<sup>18</sup>. By ab initio molecular dynamics simulation, J.M. Skelton et al. found that the change of the conduction type comes from the narrowed bandwidth and lower energy of the Bi p states compared to those of Sb. This leads to a shift of the valence and conduction band edges to lower energies with increasing Bi content<sup>19</sup>. In addition, a reverse change in the p-to-n conduction type has also been observed in Bi-doped thermoelectric Ge-Te-Bi materials<sup>20</sup>, resulting in the composition-dependent Seebeck coefficient changing from positive to negative with respect to the doping concentration.

While the mechanism of conduction is still arguable in various materials, observation of Bi-doped Zn-Sb at the atomic scale could be helpful for understanding how Bi can affect the electrical transport. In this work, we

demonstrate the impact of Bi doping on the microstructure of  $\text{Zn}_2\text{Sb}_3$  films using a Cs-corrected scanning transmission electron microscope (STEM). We perform a detailed experimental study of the effect of Bi doping on the microstructure, crystallization behavior, and electrical properties of  $\text{Zn}_2\text{Sb}_3$  alloys. In particular, we focus on how the dopant integrates into the host structure and on the role of a spinodal decomposition process in the enhancement of the crystallization behavior. Overall, the results explain how the different phases can tune the conversion of p–n type conduction in Bi-doped phase-change materials. The general methods employed in this work should be applicable to the study of other related materials.

## Materials and methods

### Film preparation

Bi-doped  $\text{Zn}_2\text{Sb}_3$  films with a thickness of  $\sim 200$  nm were deposited at room temperature on quartz and  $\text{SiO}_2/\text{Si}$  (100) substrates by the magnetron cosputtering method using individual  $\text{Zn}_2\text{Sb}_3$  and Bi targets. The substrate temperature was kept at room temperature. In each run of the experiment, the base and working pressures in the chamber were set to  $5.6 \times 10^{-4}$  and 0.3 Pa, respectively. The Ar gas flow was set to 47.6 mL/min. The radio frequency power ( $P_{\text{rf}}$ ) applied to the  $\text{Zn}_2\text{Sb}_3$  target was fixed at 50 W, while the direct current power ( $P_{\text{dc}}$ ) applied to the Bi target was varied among 0, 1, 2, 3, 4, 5, and 6 W to tune the amount of Bi in the  $\text{Zn}_2\text{Sb}_3$  films. The as-prepared samples were thus labeled as ZSB0 ( $\text{Zn}_2\text{Sb}_3$ ), ZSB1 ( $(\text{Zn}_2\text{Sb}_3)_{96.8}\text{Bi}_{3.2}$ ), ZSB2 ( $(\text{Zn}_2\text{Sb}_3)_{94.6}\text{Bi}_{5.4}$ ), ZSB3 ( $(\text{Zn}_2\text{Sb}_3)_{91.8}\text{Bi}_{8.2}$ ), ZSB4 ( $(\text{Zn}_2\text{Sb}_3)_{86.7}\text{Bi}_{13.3}$ ), ZSB5 ( $(\text{Zn}_2\text{Sb}_3)_{82.7}\text{Bi}_{17.3}$ ) and ZSB6 ( $(\text{Zn}_2\text{Sb}_3)_{75.9}\text{Bi}_{24.1}$ ), respectively, and their compositions measured by energy dispersive spectroscopy (EDS, Tescan VEGA 3 SBH, Czech Republic) are listed in Supplementary Table S1. The as-prepared amorphous samples were annealed in a vacuum oven at various temperatures between  $200^\circ\text{C}$  and  $350^\circ\text{C}$  for a holding time of 10 min. The samples deposited on quartz and  $\text{SiO}_2/\text{Si}$  (100) substrates with sizes of  $1 \times 1$  cm were used for X-ray diffraction and electrical measurements, respectively. Thirty nanometer-thick  $\text{Zn}_2\text{Sb}_3$  and Bi-doped  $\text{Zn}_2\text{Sb}_3$  thin films were directly deposited on TEM grids coated by carbon thin film at room temperature.

### Film characterization

The sheet resistances of the as-deposited films as a function of elevated temperature (nonisothermal) and time at a specific temperature (isothermal) were measured in situ using a four-probe method in a homemade vacuum chamber under the protection of Ar gas at a heating rate of 40 K/min. The crystallization of the samples was examined by X-ray diffraction (XRD, D2 Phaser, Bruker, Germany) with Cu  $K\alpha$  radiation ( $\lambda = 0.154$  nm, 36 kV, 20 mA). X-ray photoelectron spectroscopy (XPS, AXIS

ULTRA DLD) was used to probe the chemical bonding states of the elements. Advanced STEM measurements were performed with a probe Cs-corrected Titan<sup>3</sup> G2 60-300 microscope equipped with a high-angle annular dark-field (HAADF) detector and a Super-X EDX system. A probe-forming aperture of 25 mrad was used during the experiments. The elemental mapping was acquired in STEM mode using a 200 pA beam current. The TEM was operated at a 300 kV accelerating voltage. The carrier type, concentration and mobility of the crystalline films were measured using conventional Hall measurements (HP-5500C, Nanometrics, USA). The electrical resistivity ( $\rho$ ) and the Seebeck coefficient ( $S$ ) were measured in situ using a thin-film thermoelectric parameter test system (MRS-3M, Wuhan Giant Instrument Technology Co., LTD). The power factor (PF) was calculated using  $PF = S^2/\rho$ <sup>21</sup>.

## Results and discussion

### Microstructure evolution

We first examined the chemical compositions using EDX measurements of different specimen regions since it is important to know whether thermal annealing alters the chemical compositions of  $Zn_2Sb_3$  samples. The structural and chemical identification of the as-deposited and 200 °C-annealed  $Zn_2Sb_3$  films (Supplementary Fig. 1) reveals the composition uniformity and confirms the amorphous structure without any precipitation of a crystalline phase. When the film is annealed at 250 °C, the amorphous  $Zn_2Sb_3$  film begins to crystallize and gradually forms two different crystalline areas corresponding to the gray (I) and bright (II) areas in the BF-TEM image shown in Fig. 1a. The grains of area II are enclosed by the grains of area I. From the selected area electron diffraction (SAED) patterns taken from areas I and II, the metastable orthorhombic ZnSb and trigonal Sb phases, respectively, are identified. The discontinuous and separated spots of the polycrystalline rings in the SAED patterns imply large crystal grains. The grain structure can be further determined by high-resolution transmission electron microscopy (HRTEM) imaging, as shown in Fig. 1b, c. The interplanar distance suggests that area I in Fig. 1b exhibits the [310] orientation of the metastable orthorhombic ZnSb structure. It is also found that another single-crystal grain with the [104] orientation separated by some disorder features is present in area II, as shown in Fig. 1c. From the lattice distance, these small grains can be ascribed to the crystalline Sb phase. These results suggest that phase separation occurred in the 250 °C-annealed  $Zn_2Sb_3$  film (metastable orthorhombic ZnSb and trigonal Sb phases).

Z-contrast imaging allows us to study phase separation with high spatial resolution. Figure 1d presents an HAADF micrograph of the 250 °C-annealed  $Zn_2Sb_3$  thin film. The image shows areas with bright (area I), less bright (area II) and dark contrasts. By measuring three

different positions located in areas I and II of the TEM specimen, the average compositions of areas I and II can be identified as  $Zn_{54.2}Sb_{45.8}$  and  $Zn_{26.8}Sb_{73.2}$ , respectively. Obviously, a higher annealing temperature induces composition segregation and thus affects the crystallization behavior. Figure 1e presents the Sb elemental mapping image, while Fig. 1f shows the Zn elemental mapping. The bright regions in Fig. 1d can be attributed to the ZnSb phase, whereas the less bright region in Fig. 1d is a Sb-rich phase. Although some Zn diffuses into the Sb-rich phase, close inspection of the dark areas reveals the formation of Zn-rich Sb precipitates. To accurately confirm the crystal type in area II, the blue rectangular area in Fig. 1d is enlarged as shown in Fig. 1g–i. The Sb elemental mapping in Fig. 1g exhibits features similar to those in the blue rectangular area in Fig. 1d. It is evident that the crystals belong to the Sb phase with a good distribution of Sb element and diffusion-induced dark areas. In Fig. 1h, Zn atoms fill the dark areas in area II, which is more clearly observed in Fig. 1i.

Crystalline area I gradually grows during annealing of the  $Zn_2Sb_3$  thin film at a temperature of 300 °C in the BF-TEM image (Fig. 2a). The film again separates into a mixture of areas I and II. However, the grains of area II are disconnected from each other, forming crystalline domains. The SAED images taken from areas I and II show the formation of metastable ZnSb and Sb phases (Fig. 2b, c), respectively. In addition, nanosized regions with very bright contrast (see the red arrows) appear within the ZnSb phase (Fig. 2a, b).

The element distribution in 300 °C-annealed  $Zn_2Sb_3$  films was further studied by HAADF (Fig. 2d) and EDX elemental mapping (Fig. 2e–g). From the HAADF and EDX maps, it was concluded that the bright contrast in the BF-TEM image comes from disordered regions inside the  $Zn_2Sb_3$  thin film. These regions were attributed to holes in the thin film. Figure 2d shows a boundary between areas I ( $Zn_{54.6}Sb_{45.4}$ ) and II ( $Zn_{24.5}Sb_{75.5}$ ). Area I contains nanocrystals with many holes embedded at the grain boundaries of the metastable ZnSb phase (see the red arrows), while area II contains Sb-rich nanocrystals without holes. According to the Sb and Zn mapping images shown in Fig. 2e, f, many small holes can be clearly detected in area I. The formation of holes originates from out-diffusion of Zn and Sb. The out-diffusion results in the formation of Zn-rich and Sb-rich nanoprecipitates in areas I and II, respectively, which is more clearly observed in Fig. 2g.

Interestingly, holes are not formed in the stable ZnSb phase during thermal annealing of the  $Zn_2Sb_3$  thin film at a temperature of 350 °C. Figure 3a shows a BF-TEM image of the 350 °C-annealed film. Again, two crystalline areas are evident from the image. SAED patterns taken from areas I and II are shown as insets in Fig. 3b, c. The film crystallizes into a mixture of the stable trigonal ZnSb phase (area I) and

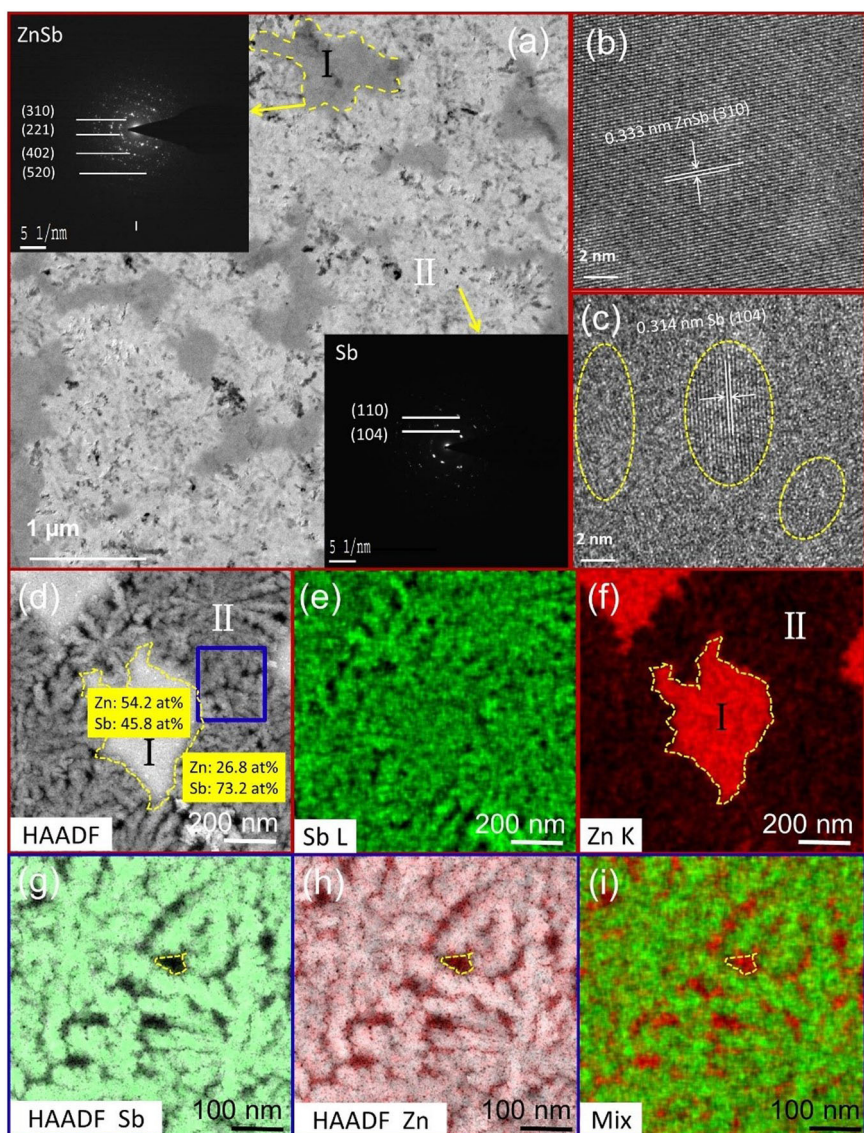


**Fig. 1** Structural and chemical identification of 250 °C-annealed  $\text{Zn}_2\text{Sb}_3$  film. **a** BF-TEM image and SAED images; **b, c** HRTEM images of selected areas I and II. **d** HAADF micrograph; respective elemental mapping for individual **e** Sb and **f** Zn. Enlarged HAADF micrographs of individual **g** Sb and **h** Zn and **i** mixed Zn and Sb in the selected blue rectangular region.

Sb phase (area II). Thus, the crystal structure in area I is believed to transform into a new crystal structure, while the crystal structure ascribed to the Sb phase in area II remains unchanged. However, the crystal size of the ZnSb phase decreases (20–30 nm) compared to those in the 250 °C- and 300 °C-annealed thin films. The holes may provide space for the rearrangement of atoms during the phase transition from the metastable to stable ZnSb phase<sup>22</sup>.

The distribution of chemical elements in the 350 °C-annealed  $\text{Zn}_2\text{Sb}_3$  thin film is shown in the HAADF micrograph (Fig. 3d), where three areas can be identified. Areas I ( $\text{Zn}_{49.3}\text{Sb}_{50.7}$ ) and II ( $\text{Zn}_{32.6}\text{Sb}_{67.4}$ ) are ZnSb and Zn-doped Sb phases, respectively. The third area is Zn

precipitates within area II. Compared to previous samples, the distribution of the Zn doping element in area II is more uniform. On the other hand, the size of Zn grains in area II is larger compared with those in the previous samples. The possible situations can be ascribed to the fact that a higher annealing temperature leads to distinct element diffusion. The Sb elemental mapping in Fig. 3e indicates that a large amount of Sb diffuses towards area I and accumulates in the dark-green area, leading to more and larger dark cavities in the bright-green II area. The Sb diffusion direction is opposite to that in the 300 °C-annealed film. Similarly, in Fig. 3f, a large amount of Zn diffuses in the same direction to area I and accumulates in

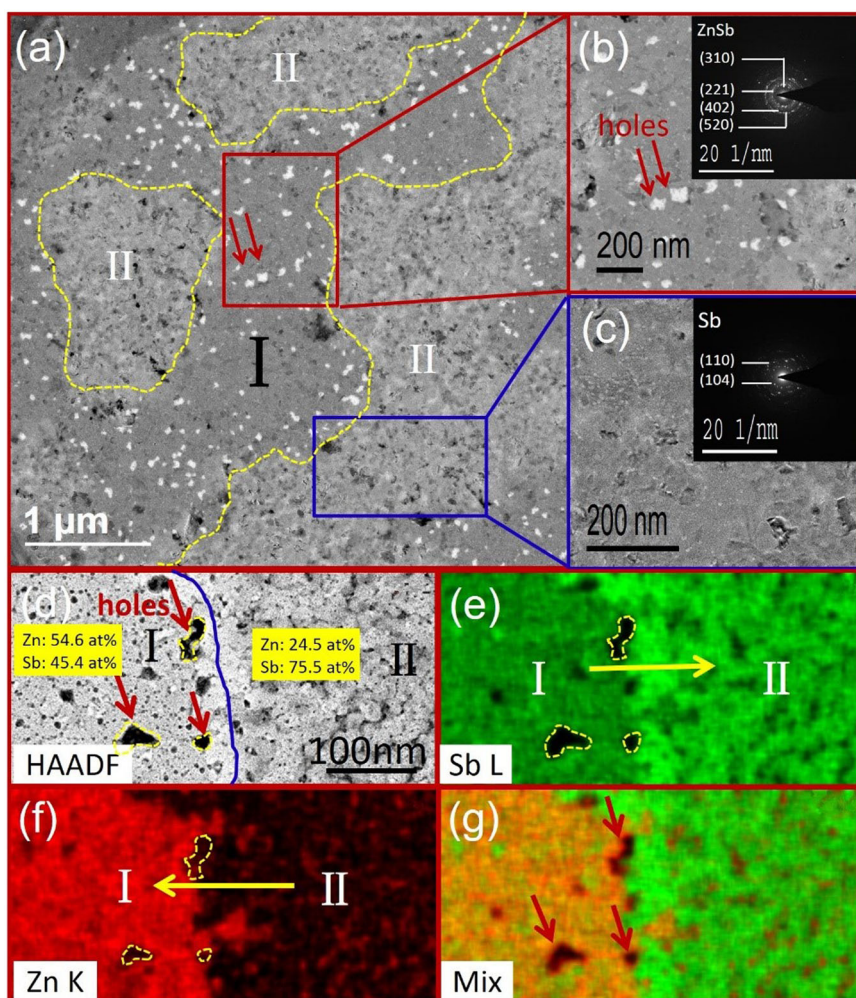


**Fig. 2** Structural and phase separation of 300 °C-annealed  $\text{Zn}_2\text{Sb}_3$  film. **a** BF-TEM image; respective enlarged BF-TEM and inset SAED images for areas **b** I and **c** II. **d** HAADF micrograph of 300 °C-annealed  $\text{Zn}_2\text{Sb}_3$  film; respective elemental mapping for individual **e** Sb and **f** Zn and for **g** mixed Zn and Sb.

the bright-red area, but no cavity caused by Zn diffusion is found anywhere in the dark-red II area. Thus, a large amount of Zn and Sb elements finally accumulate in area I. The ratio of Zn and Sb is close to 1:1 in area I. Note that the grain sizes are clearly reduced, and no cavity is found anywhere. Subsequently, in the mixed element mapping image of Fig. 3g, one can find that the distribution of Zn and Sb elements is uniform in left area I, while in right area II, some of the Zn fills in the cavities. This suggests that the metastable  $\text{ZnSb}$  phase completely converts into a new crystalline phase with a stable  $\text{ZnSb}$  structure. The crystal in area II is still the Sb phase surrounded by more Zn precipitates compared with that in the 300 °C-annealed film. Obviously, all these significant changes are due to element diffusion, which plays an important role in the phase separation mechanism of  $\text{Zn}_2\text{Sb}_3$  films during the phase change process. The two-step phase transition of

the films is directly confirmed by STEM and will be further evidenced by the changes in the electrical properties.

#### Properties and microstructure of Bi-doped $\text{Zn}_2\text{Sb}_3$ thin films

The sheet resistances in Bi-doped  $\text{Zn}_2\text{Sb}_3$  thin films as a function of temperature ( $R-T$ ) are shown in Fig. 4a.  $T_c$  rapidly decreases with increasing Bi content and is 229 °C for ZSB1, 163 °C for ZSB2, 150 °C for ZSB3, 147 °C for ZSB4, 120 °C for ZSB5 and 100 °C for ZSB6 (Supplementary Table S1). Interestingly, the sheet resistance behavior in Bi-doped  $\text{Zn}_2\text{Sb}_3$  films differs from that in the undoped  $\text{Zn}_2\text{Sb}_3$  alloy (Supplementary Fig. S2). When the Bi concentration is between 5.4 and 13.3 at%, there is a gradual change in the sheet resistance across the crystallization temperatures for the ZSB2, ZSB3 and ZSB4 films, which is in contrast to the abrupt change for the ZSB0

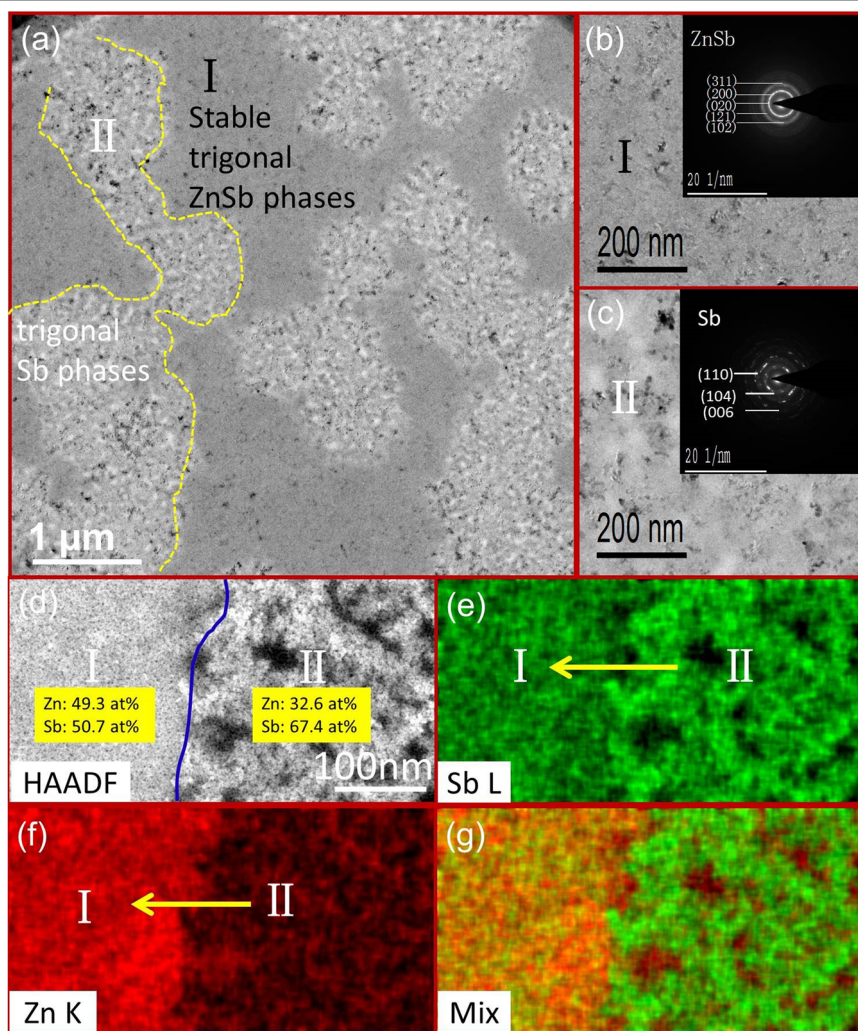


**Fig. 3** Microstructure characterization of 350 °C-annealed  $\text{Zn}_2\text{Sb}_3$  film. **a** BF-TEM image; respective enlarged BF-TEM and inset SAED images for areas **b** I and **c** II. **d** HAADF micrograph of 350 °C-annealed  $\text{Zn}_2\text{Sb}_3$  film; respective element mapping for individual **e** Sb and **f** Zn and **g** mixed Zn and Sb.

and ZSB1 samples. This indicates a changing phase-change ability, which is believed to come from a change in the crystallization processes. When the Bi-doping concentration is further increased to above 13.3 at%, the ZSB5 and ZSB6 films exhibit continuous crystallization and sheet resistance changes with increasing annealing temperature. The high Bi concentration lowers the crystallization temperature and facilitates easier crystallization. This may be due to an increase in the free volume in the amorphous material and a corresponding decrease in viscosity, facilitating easier atomic diffusion during crystallization<sup>23</sup>. On the other hand, the resistance of the amorphous state decreases with Bi doping, while the resistivities in the crystalline states have comparable values (these states are already highly conductive, and hence, doping has little effect). Among the Bi-doped  $\text{Zn}_2\text{Sb}_3$  films, the ZSB1-ZSB4 thin films have high

resistance ratios between the amorphous and crystalline phases, ranging between two and three orders of magnitude (Fig. 4b). These values are advantageous for applications in phase-change storage devices.

The data retention was measured using the Arrhenius equation:  $t = \tau \exp(E_a/k_B T)^{24}$ , where  $\tau$  is a proportional time constant. The failure time ( $t$ ) is defined as the time at which the resistance decreases to half of its initial value at a specific temperature ( $T$ ). As shown in Fig. 4c, the temperature for the 10-year data retention of the ZSB0 sample is 220 °C, while that for ZSB1 is reduced to 119 °C with the addition of Bi. This is correlated with the decreased thermal stability. Bi doping reduces the activation energy of  $\text{Zn}_2\text{Sb}_3$  from 8.71 to 2.14 eV at 3.2 at% dopant. This behavior is in good agreement with other studies<sup>19,25</sup>. Excessively high Bi-doping concentrations can degenerate the phase-change ability while leading to partial

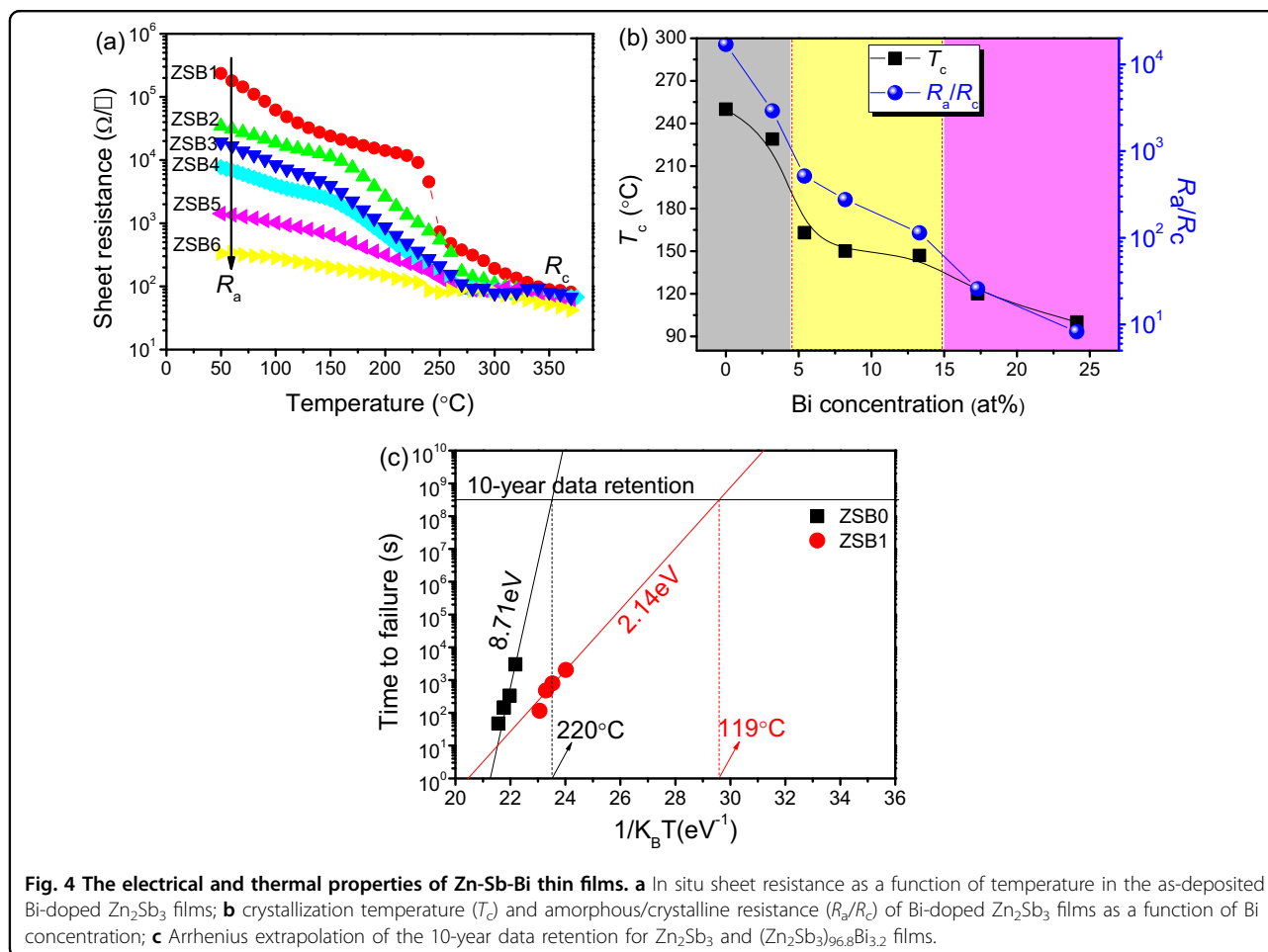


**Fig. 4** The electrical and thermal properties of Zn-Sb-Bi thin films. **a** In situ sheet resistance as a function of temperature in the as-deposited Bi-doped  $\text{Zn}_2\text{Sb}_3$  films; **b** crystallization temperature ( $T_c$ ) and amorphous/crystalline resistance ( $R_a/R_c$ ) of Bi-doped  $\text{Zn}_2\text{Sb}_3$  films as a function of Bi concentration; **c** Arrhenius extrapolation of the 10-year data retention for  $\text{Zn}_2\text{Sb}_3$  and  $(\text{Zn}_2\text{Sb}_3)_{96.8}\text{Bi}_{3.2}$  films.

crystallization in the as-deposited ZSB4-6 samples, as revealed by XRD and TEM (Supplementary Figs. S3–S4).

#### Real space investigations of crystal structure transformation

Figure 5 shows TEM and corresponding SAED and HRTEM images of the ZSB1, ZSB2 and ZSB4 films annealed at  $300^{\circ}\text{C}$ . The ZSB1 film with a low Bi concentration shows a typical dual-phase structure (Fig. 5a) with uniformly distributed nanocrystals. The grain size is  $\sim 20$ – $30$  nm. When the Bi content is increased to 5.4 (ZSB2) and 13.3 at% (ZSB4), the metastable grains become continuously larger, up to  $\sim 50$  and  $100$  nm (Fig. 5b, c), respectively. This illustrates that the more Bi atoms are doped, the larger the crystal grains are. The reason is that the dominant metastable phase quickly engulfs adjacent small grains and grows into a larger phase, as clearly recorded in the TEM images at higher temperatures<sup>26</sup>.

At the same time, the SAED patterns illustrate that the crystal structure of  $\text{Zn}_2\text{Sb}_3$  has changed due to Bi doping. The annealed Bi-doped  $\text{Zn}_2\text{Sb}_3$  films are all in polycrystalline states, as suggested by the SAED patterns (Fig. 5a1–a2, b1–b2, and c1–c2). The ZSB1 film shows a

typical dual-phase structure, as indexed in Fig. 5a3, which crystallizes into metastable ZnSb (A) and Sb (B) phases. When the Bi doping is further increased, the metastable grains become continuously larger (Fig. 5a1–c1), and thus, the diffraction rings become slightly discontinuous. A new crystalline (Bi,Sb) phase can be found in Fig. 5b2–c2. According to the HRTEM images (Fig. 5b3–c3), the corresponding distributions are converted into metastable ZnSb (A) and (Bi,Sb) (C) phases for the ZSB2 and ZSB4 samples. To further confirm this result, the red and yellow regions in Fig. 5c3 were selected and are enlarged in Fig. 5c4–c5. The lattice spacing between the crystallographic planes in Fig. 5c4 corresponds to the value for the metastable ZnSb structure. In addition, the measured d-spacing (0.312 nm) in Fig. 5c5 matches the [012] zone axis in the crystalline (Bi,Sb) phase very well. This indicates that the crystallized film includes the rhombohedral (Bi,Sb) phase, which precipitates from the Sb(Bi) matrix when more Bi atoms are added. The formation of Sb-Bi phases has also been further confirmed by XPS (Supplementary Fig. S5). The TEM investigations strongly support the notion that a unique dual-phase structure is formed in Bi-doped  $\text{Zn}_2\text{Sb}_3$  films.

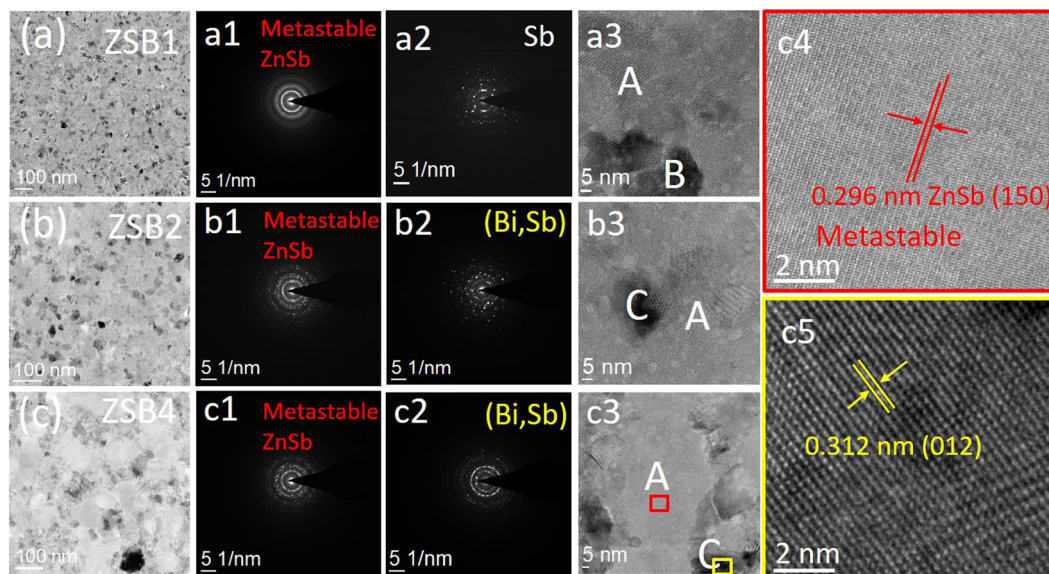


**Fig. 5** Microstructure characterization of ZSB1-ZSB4 thin films. TEM images of **a** ZSB1, **b** ZSB2 and **c** ZSB4 annealed at 300 °C. The corresponding SAED patterns of ZSB1, ZSB2 and ZSB4 are shown in **a1–a2**, **b1–b2** and **c1–c2**, respectively. The corresponding HRTEM images of ZSB1, ZSB2 and ZSB4 are shown in **a3**, **b3** and **c3**, where A–C represent distributions of metastable ZnSb, Sb, and Bi-Sb precipitates, respectively. The selected rectangular regions in **c3** for A (red) and C (yellow) are enlarged and displayed in **c4** and **c5**, respectively.

The ZSB4 thin film annealed at a higher temperature of 350 °C was also examined. Clear grain boundaries and interfaces can be observed in Fig. 6a. The SAED patterns shown in Fig. 6b, c represent distinguishable diffraction patterns, which correspond to the Bi-Sb phase (C) and stable ZnSb phase (D) in Fig. 6d. Compared to the 300 °C-annealed ZSB4 sample, the TEM data strongly support that the metastable orthorhombic ZnSb phase is converted into the stable trigonal ZnSb phase after a short period of heating at 350 °C. It should be noted that the stable ZnSb phase is produced at higher temperatures. Therefore, the combination of annealing temperature and composition can provide a rich platform to tailor the intermediate metastable phase-change process and reveal the crystallization origin.

Overall, in the pure crystalline  $\text{Zn}_2\text{Sb}_3$  (ZSB0) thin film, Zn-Sb and Sb phases are formed and segregate into compositionally divergent nanoscale domains during thermal heating, as confirmed by the STEM images. The microstructural observations of Zn-Sb-Bi (ZSB1-4) demonstrate spinodal-like decomposition of Zn-Sb-Bi alloy after the annealing process. The main crystalline phases (Sb and ZnSb) in the ZSB1 film with 20–30 nm domains are precipitated. The Sb phase is gradually transformed into the (Bi,Sb) phase as the Bi-doping concentration is increased to 5.4 at%, while the ZnSb phase remains unchanged. This indicates that the ZnSb phase is more thermodynamically and chemically stable than the Sb phase at higher doping concentrations, although some Bi atoms are introduced into the phase. As the

concentration of Bi is increased to 13.3 at% (ZSB4), the precipitated phases (ZnSb and (Bi,Sb)) are unchanged. These observations validate that the phase decomposition of Zn-Sb-Bi alloy can only originate from thermally induced element diffusion and are a fingerprint of spinodal decomposition. Moreover, the HRTEM observations in Fig. 6e, f reveal that spinodal decomposition begins at interfaces between the Zn-Sb and Bi-Sb grain boundaries, indicating that the spinodal decomposition has a surface-directed component<sup>27</sup>.

#### Impact of doping on spinodal decomposition

To provide better direct experimental evidence for spinodal decomposition, a series of STEM-HAADF images were recorded of the intermediate structure of ZSB1-ZSB4 films annealed at 300 °C. For ZSB1, the HAADF image shows that crystalline grains with a size of several tens of nanometers are uniformly distributed in the film (Fig. 7a). Fig. 7a1–a3 present the Sb, Zn, and Bi elemental mapping from the same area as in Fig. 7a. Apparently, the Sb element is uniformly distributed in the whole crystalline area, while Zn and Bi elements are precipitated and separated from each other (Fig. 7a4). The sample displays an irregular and varying structure, in contrast to the as-deposited homogeneous film (not shown here), consistent with compositional fluctuations. Thus, the original ZSB1 has been segregated into two pronounced nanoscale domains of Zn-Sb and Bi-Sb compositions as a result of spinodal-like decomposition. With increasing Bi-doping concentration from 5.4 to



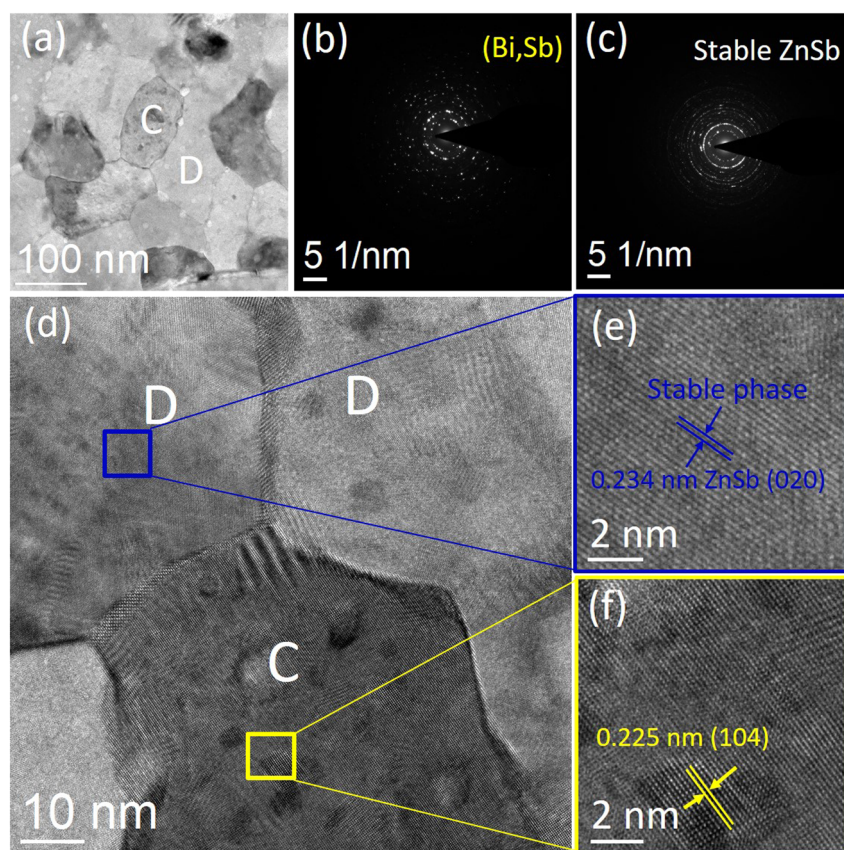


**Fig. 6** Microstructure characterization of ZSB4 annealed at 350 °C. **a** TEM image where the selected crystals C and D are indexed by the SAED patterns shown in **b** and **c**. The corresponding HRTEM image is shown in **d**, where the blue and yellow regions are selected to determine the lattice spacing of the crystals and are enlarged in **e** and **f**.

13.3 at%, the decomposition behavior in the 300 °C-annealed ZSB2-ZSB4 films is obvious, and the separated areas become larger, as shown in Fig. 7b–d. The uniform green color in Fig. 7a1–d1 indicates that Sb is uniformly distributed throughout the entire crystalline region, while the red elements in Fig. 7a2–d2 indicate that Zn is dominant in the black-gray crystalline area. In contrast, the blue Bi elemental mapping across the entire region shows that Bi only disperses in the white-gray crystalline area, as shown in Fig. 7a3–c3. This also illustrates that there is no intermixing between the Zn and Bi elements (Fig. 7a4–d4) during the phase separation process. Thus, the crystalline phases are dominated by mixtures of Zn-Sb and Bi-Sb phases, which are well dispersed in the black-gray and white-gray crystalline areas, respectively. The material undergoes composition segregation through spinodal-like decomposition during the growth of Zn-rich Zn-Sb and Sb-rich Bi-Sb domains. When the Bi content is increased to 13.3 at% (ZSB4), these clusters then rapidly grow and coalesce until they form Zn-Sb clusters and Bi-Sb clusters. The compositions of the gray and bright areas of the ZSB2 sample were measured to

be 51 at% Sb, 0 at% Bi, and 49 at% Zn (see yellow rectangle) and 74.8 at% Sb, 4.3 at% Bi and 20.9 at% Zn (see white rectangle), respectively. Additionally, the compositions of the gray and bright regions in the ZSB4 sample were found to be 46.5 at% Sb, 0.4 at% Bi and 53.1 at% Zn and 13.3 at% Zn, 62.7 at% Sb and 24.0 at% Bi, respectively. Thus, the original Zn-Sb-Bi decomposes into different phases, similar to the spinodal decomposition process. This decomposition becomes even more pronounced with increasing Bi concentration, where two completely distinct Zn-Sb and Sb-rich Bi-Sb crystalline regions form.

In the case of spinodal phase separation, any small composition fluctuation can lead to Zn-rich regions (becoming richer in ZnSb) and Sb-rich regions (becoming richer in Bi-Sb). This is because such a process causes a decrease in the free energy. Thus, this is direct experimental evidence for spinodal decomposition in the Zn-Sb-Bi system, which is driven by atom diffusion. Upon spinodal decomposition, the Bi-Sb domains formed in the ZSB4 film at 300 °C can also grow with increasing temperature (Supplementary Fig. S6).

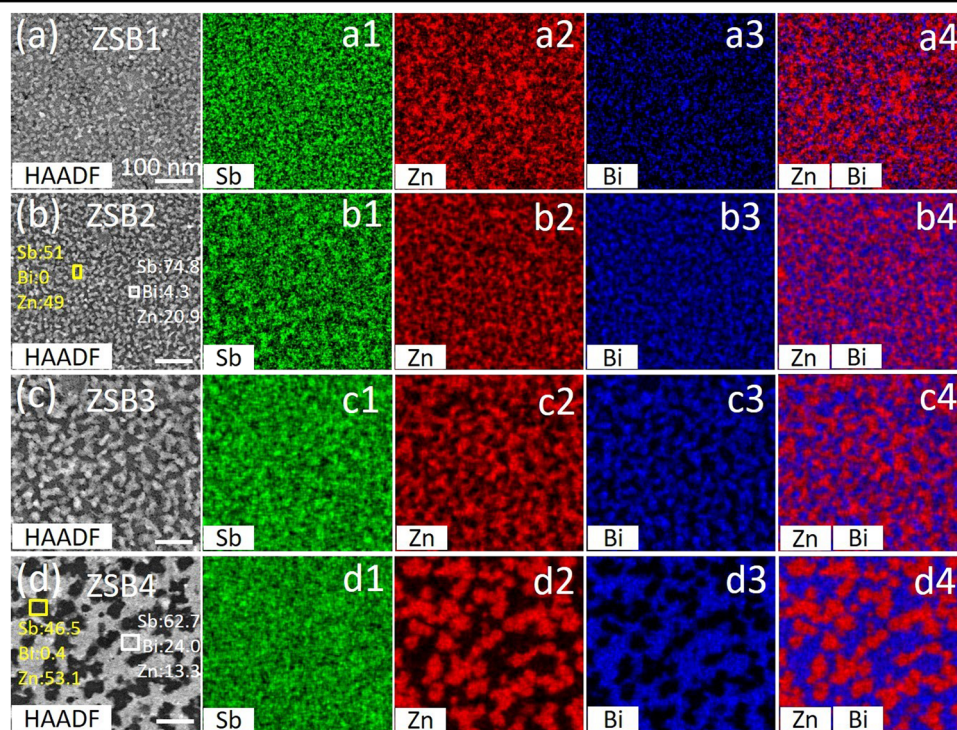


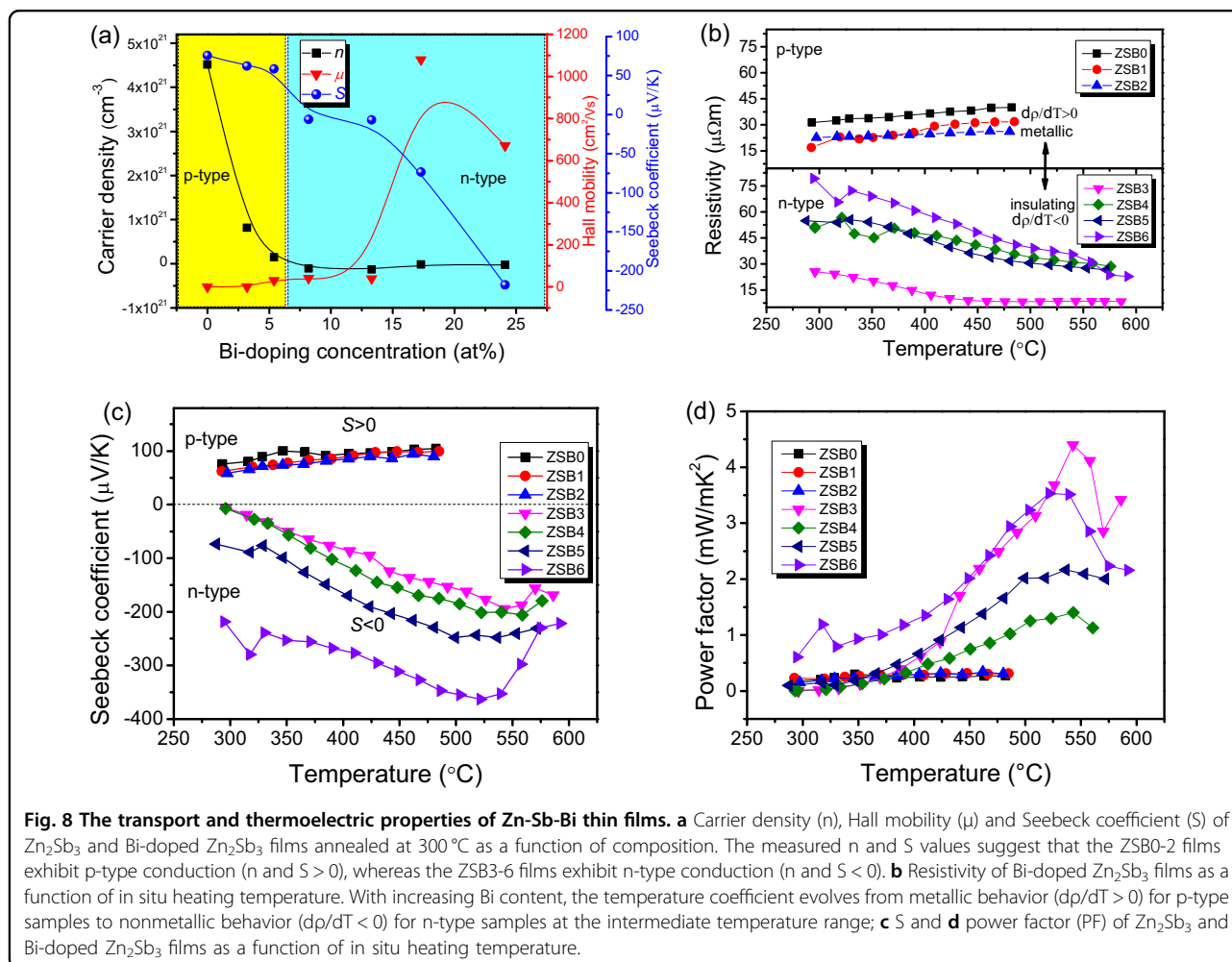
**Fig. 7** ZSB1-4 films annealed at 300 °C with heterojunction networks exhibiting spinodal-like decomposition morphologies and corresponding evolution of the chemical compositions. **a–d** STEM-HAADF images; corresponding EDX measured element distribution maps of **a1–d1**: Sb (green), **a2–d2**: Zn (red) and **a3–d3**: Bi (blue). **a4–d4** represent the mixed distribution of Zn and Bi. The scale bars in the HAADF images are 100 nm.

### Transport properties and metal-insulator transition

Two important parameters of the electrical properties of semiconductors are the carrier concentration and mobility. The electrical transport properties are estimated from the Hall Effect Test System measurements for the 300 °C-annealed Bi-doped  $\text{Zn}_2\text{Sb}_3$  films, as shown in Fig. 8a. To carry out the Hall measurements, these films with a  $1 \times 1 \text{ cm}^2$  area were used. The Hall measurements reveal that the pure  $\text{Zn}_2\text{Sb}_3$  film annealed at 300 °C has a carrier density of  $4.52 \times 10^{21} \text{ cm}^{-3}$  and a mobility of  $0.175 \text{ cm}^2/\text{Vs}$ , while the Bi-doped ZSB1 sample exhibits slightly lower carrier density and mobility of  $8.18 \times 10^{20} \text{ cm}^{-3}$  and  $0.174 \text{ cm}^2/\text{Vs}$ , respectively. The quite low mobility might be due to intrinsic defects present in the compounds. The variations in the mobility and carrier concentration with the Bi concentration for the 300 °C-annealed Zn-Sb-Bi films are summarized in Supplementary Table S1. The positive sign of the carrier density reveals that the crystalline  $\text{Zn}_2\text{Sb}_3$  films with low Bi doping are p-type in nature, but a higher Bi-doping level changes the conduction from p- to n-type. Zn vacancies are one of the main contributors to p-type doping in crystalline Zn-Sb alloys<sup>28</sup>. With an increase in the Bi concentration, the Zn vacancies are reduced, leading to a lower p-type doping concentration and thus a lower carrier density. As reported, single crystal Sb was found to be a

p-type semiconductor in crystalline  $\text{ZnSb-Sb}_2\text{Te}_3$  alloys<sup>29</sup>. Additionally, crystalline ZnSb was considered as a p-type semiconductor with Zn acting as a dopant<sup>30</sup>. Thus,  $\text{Zn}_2\text{Sb}_3$  films with lower Bi-doping concentration can only be a p-type semiconductor after the abovementioned annealing treatment due to the formation of Sb and ZnSb crystals, where an increase in the Bi content leads to a lower carrier density than that of  $\text{Zn}_2\text{Sb}_3$ . However, the situation is different for the thin films with higher Bi-doping concentrations. With more Bi addition, Bi will bond with Sb, forming more Bi-Sb crystalline phases in the Zn-Sb-Bi alloys. This has been confirmed by TEM/XRD measurements. The conduction type of these alloys transitions from p-type for the undoped  $\text{Zn}_2\text{Sb}_3$  to n-type semiconducting as n-type Bi-Sb<sup>31</sup> becomes dominant in the crystalline Zn-Sb-Bi alloys.

Additionally, the resistivity ( $\rho$ ) of the Zn-Sb-Bi thin films changes with temperature and Bi-doping concentration (Fig. 8b). The p-type crystalline ZSB0-2 films exhibit low resistivity, while the relatively high resistivity observed for the n-type  $\text{Zn}_2\text{Sb}_3$  films with high Bi-doping concentration (SZB3-6) is due to the formation of the additional Bi-Sb phase<sup>26,31</sup>. The Bi-Sb phase appears to be important in determining the properties of Zn-Sb-Bi alloy because the size of the Bi-Sb grains (80–110 nm) becomes comparable to or larger than that of Zn-Sb grains



(70–90 nm) with increasing Bi doping, as evaluated by TEM data. The larger crystallite size formed in high Bi-doped samples after annealing reduces grain boundary scattering and increases the mobility of the films. The increase in mobility may also be due to the improvement in the crystallinity of the films with annealing.

We propose that such  $\rho$  dependences can be interpreted in terms of inhomogeneous transport. Evidence comes from the existence of two ZnSb and Bi-Sb crystals as determined by TEM. In the nanocrystalline film with heterojunction networks, both phases are regularly separated from each other. This promotes the thermal and electronic transport of the carriers, resulting in good phase-change and thermoelectric properties. Among all possible ternary components of multicomponent Zn-Sb-Bi films, ZSB3-6 with n-type conduction contain self-organized heterojunction networks where Bi-Sb is dominant during crystallization. Thus, assuming that inhomogeneous transport plays a major role in the systems, the appearance of n-type conduction starts in the vicinity of the percolation threshold where these

components are dominant. For instance, we observe a significant increase in the conductivity of the ZSB3 film after annealing in Fig. 8b. This may be further experimental proof of the p- to n-type conduction conversion caused by the heterojunction structure.

In addition, a gradual metal-insulator transition in p-type and n-type Bi-Zn-Sb films can be observed in Fig. 8b, which is reminiscent of the behavior seen by Siegrist et al.<sup>32</sup> and Volker et al.<sup>33</sup>. The question of whether the films are metallic or insulating, i.e., whether the temperature coefficient of resistivity has a negative or positive slope, can only be answered by proper  $dp/dT$  extrapolations. In the critical region, i.e., close to the metal-insulator transition (MIT) point,  $dp/dT$  typically obeys the following behaviors, where  $dp/dT > 0$  and  $dp/dT < 0$  indicate metallic and insulating behaviors, respectively<sup>34</sup>. As shown in Fig. 8b, the films with low Bi-doping concentrations (ZSB0-2) display  $dp/dT > 0$ , and they are clearly metallic. In contrast, the films with high Bi-doping concentration (ZSB3-6) are insulating. Thus, we observe an MIT with increasing Bi-doping concentration from 0

to 13.3 at%. This can be explained in terms of the coexistence of an insulating rhombohedral Bi-Sb phase<sup>31</sup> and a metallic trigonal ZnSb phase<sup>35</sup>. The Bi-Sb insulator gradually becomes dominant with higher Bi-doping concentration, and the amount of the ZnSb phase decreases. These observations demonstrate that the combination of the annealing temperature and stoichiometry, therefore, provides a platform to tailor the crystallization process and material properties. The Zn-Sb-Bi films have the characteristic of an MIT, which provides another way to achieve multilevel data storage.

Meanwhile, the MIT behavior can enhance the thermoelectric properties of Bi-modified Zn<sub>2</sub>Sb<sub>3</sub> for applications in novel thermoelectric devices. We measured the Seebeck coefficient (*S*) and power factor (PF) of crystalline Zn<sub>2</sub>Sb<sub>3</sub> and Bi-doped Zn<sub>2</sub>Sb<sub>3</sub> films, as presented in Fig. 8c, d. In general, *S* slightly decreases for p-type films, while *S* increases with increasing Bi concentration and exhibits a negative value for n-type conducting behavior during the entire MIT process. This is attributed to the phase transition from Sb to Bi-Sb and from the metastable to stable ZnSb phase during the critical phase transition of the MIT behavior. Influenced by critical scattering, the Seebeck coefficient and the electrical resistivity sharply increase. Thus, the PF value rapidly increases. For Zn<sub>2</sub>Sb<sub>3</sub> films with low Bi-doping concentration (ZSB1-2), the *S* values exhibit a similar dependence on the dominant ZnSb single crystals. Since crystalline ZSB1-2 films can be obtained by heating, the films should partially or fully evolve into stable ZnSb nanocrystals during TE property measurements. For the n-type ZSB3-5 films upon heating, the *S* and PF values increase because the dominant crystalline phase changes from ZnSb to Bi-Sb, as confirmed by XRD data, which is consistent with the behavior observed by Murmu et al.<sup>36</sup>. Combining  $\rho$  and *S*, ZSB3 exhibits good n-type conduction with a large thermoelectric PF (4.4 mW/mK<sup>2</sup> at ~540 °C) (Fig. 8d). In addition, it has been suggested that the trigonal ZnSb phase could be unstable for the ZSB6 film; thus, the ZSB6 film completely crystallizes into the stable rhombohedral Bi-Sb phase. The measured *S* (~520 °C) of the ZSB6 film reaches approximately -362.8  $\mu$ V/K, and it has a high PF value of ~3.5 mW/mK<sup>2</sup> at ~520 °C (Fig. 8d). This illustrates that high PFs have been achieved predominantly for n-type systems, which are better than those of traditional commercial thermoelectric materials, such as Bi<sub>2</sub>Te<sub>3</sub>, PbTe, SiGe, Zn<sub>4</sub>Sb<sub>3</sub> and Ni/PVDF alloys, for which the PF is on the order of several thousand  $\mu$ W/mK<sup>2</sup><sup>12,37-40</sup>. Therefore, this result is certainly interesting for high-performance phase-change and thermoelectric electronic applications, where materials with both p-type and n-type polarities are needed.

In summary, STEM experiments combined with electrical measurements were adopted to understand the diffusion-dominated spinodal decomposition process of Zn-Sb-Bi alloys. Detailed microstructure characterization reveals that

Bi doping can suppress the Sb migration behavior, avoid the formation of holes and form coexisting Zn-Sb and Bi-Sb phases during the decomposition process. The change in conduction from p- to n-type beyond a critical Bi doping level of 8.2 at% is explained by the presence of the Bi-Sb phase, which simultaneously dominates the metal-to-insulator properties of Zn-Sb-Bi thin films and therefore provides a new strategy for realizing multilevel data storage. Moreover, Bi doping improves the thermoelectric properties observed in the doped samples when the Bi-doping concentration reaches 13.3 at%, with individual properties of *S* of -362.8  $\mu$ V/K and PF of ~3.5 mW/mK<sup>2</sup> at ~520 °C. We expect that these results may also be relevant to other diffusion-dominated alloys. The insights obtained from this study should be useful in facilitating the rational selection of dopants to optimize the properties of Zn-Sb for specific memory devices, thermoelectric cooling devices and solar cell applications in the future.

#### Acknowledgements

This work was financially supported by the National Natural Science Foundation of China (Grant Nos. 61604083 and 51972176), the Natural Science Foundation of Zhejiang Province, China (Grant No. LY20F040002), the Natural Science Foundation of Ningbo City, China (Grant No. 2019A610059), and was sponsored by the K.C. Wong Magna Fund in Ningbo University.

#### Author details

<sup>1</sup>Laboratory of Infrared Materials and Devices, The Research Institute of Advanced Technologies, Ningbo University, Ningbo, Zhejiang 315211, China. <sup>2</sup>Leibniz Institute of Surface Engineering (IOM), Permoserstr. 15, D-04318 Leipzig, Germany. <sup>3</sup>Key Laboratory of Photoelectric Detection Materials and Devices of Zhejiang Province, Ningbo, Zhejiang 315211, China

#### Author contributions

G.X. Wang and A. Lotnyk performed the film preparation and STEM observation. H.Z. Shi and D.T. Shi performed the XRD measurements of the films. A. Lotnyk, G.X. Wang and R.P. Wang analyzed the experimental and theoretical results. G.X. Wang wrote the paper with help from all co-authors. A. Lotnyk and R.P. Wang finalized the paper. The project was initiated and conceptualized by G.X. Wang.

#### Conflict of interest

The authors declare that they have no conflict of interest.

#### Publisher's note

Springer Nature remains neutral with regard to jurisdictional claims in published maps and institutional affiliations.

**Supplementary information** is available for this paper at <https://doi.org/10.1038/s41427-020-0197-8>.

Received: 3 November 2019 Revised: 6 December 2019 Accepted: 9 December 2019.

Published online: 14 February 2020

#### References

- Reinsel, D., Wu, L. F., Gantz, J. F., Rydning, J. An IDC White Paper-Doc#US44413318, <https://www.seagate.com/au/en/our-story/data-age-2025>, accessed November 2018.
- Lotnyk, A., Behrens, M. & Rauschenbach, B. Phase change thin films for non-volatile memory applications. *Nanoscale Adv.* 1, 3836–3857 (2019).

3. Li, X. B., Chen, N. K., Wang, X. P., Sun, H. B. Phase-change superlattice materials toward low power consumption and high density data storage: microscopic picture, working principles, and optimization. *Adv. Funct. Mater.* 1803380 (2018).
4. Rios, C. et al. Integrated all-photonic non-volatile multi-level memory. *Nat. Photon.* **9**, 725–732 (2015).
5. Wu, W. H. et al. Multi-level storage and ultra-high speed of superlattice-like Ge<sub>50</sub>Te<sub>50</sub>/Ge<sub>8</sub>Sb<sub>92</sub> thin film for phase-change memory application. *Nano-technology* **28**, 405206 (2017).
6. Salinga, M. et al. Monatomic phase change memory. *Nat. Mater.* **17**, 681–685 (2018).
7. Hilmi, I., Lotnyk, A., Gerlach, J. W., Schumacher, P., & Rauschenbach, B. Epitaxial formation of cubic and trigonal Ge-Sb-Te thin films with heterogeneous vacancy structures. *Mater. Des.* **115**, 138–146 (2017).
8. Ding, K. Y. et al. Phase-change heterostructure enables ultralow noise and drift for memory operation. *Science* **366**, 210–215 (2019).
9. Chen, Y. M. et al. Crystallization behaviors of Zn<sub>x</sub>Sb<sub>100-x</sub> thin films for ultralong data retention phase change memory applications. *CrystEngComm* **16**, 757–762 (2014).
10. Edwards, T. G. et al. Structural transformations in amorphous crystalline phase change of Ga-Sb alloys. *J. Appl. Phys.* **114**, 233512 (2013).
11. Zou, H. et al. Improvement of the thermal stability of Sb thin film through erbium doping. *CrystEngComm* **18**, 6365–6369 (2016).
12. Sun, Y. et al. Low-cost high-performance zinc antimonide thin films for thermoelectric applications. *Adv. Mater.* **24**, 1693–1696 (2012).
13. Hughes, M. A. et al. n-type chalcogenides by ion implantation. *Nat. Commun.* **5**, 5346 (2014).
14. Park, T. J., Choi, S. Y. & Kang, M. J. Phase transition characteristics of Bi/Sn doped Ge<sub>2</sub>Sb<sub>2</sub>Te<sub>5</sub> thin film for PRAM application. *Thin Solid Films* **515**, 5049–5053 (2007).
15. Bhatia, K. I. Electrical transport in Bi doped n-type amorphous semiconductors (GeSe<sub>3.5</sub>)<sub>100-x</sub>Bi<sub>x</sub> at high pressure. *J. Non-Cryst. Solids* **59-60**, 1019–1021 (1983).
16. Elliott, S. R. & Steel, A. T. Mechanism for doping in Bi chalcogenide glasses. *Phys. Rev. Lett.* **57**, 1316 (1986).
17. Liu, Y. et al. Influence of Bi on topological self-organization in arsenic and germanium selenide networks. *J. Mater. Chem. C* **1**, 6677 (2013).
18. Borisova, Z. U. *Glassy Semiconductors*. (Plenum Press, New York, **1981**).
19. Skelton, J. M., Pallipurath, A. R., Lee, T. H. & Elliott, S. R. Atomistic origin of the enhanced crystallization speed and n-type conductivity in Bi-doped Ge-Sb-Te phase-change materials. *Adv. Funct. Mater.* **24**, 7291–7300 (2014).
20. Wu, H. J., Chen, B. Y. & Cheng, H. Y. The p-n conduction type transition in Ge-incorporated Bi<sub>2</sub>Te<sub>3</sub> thermoelectric materials. *Acta Mater.* **122**, 120–129 (2017).
21. He, J. & Tritt, T. M. Advances in thermoelectric materials research: looking back and moving forward. *Science* **357**, eaak9997 (2017).
22. Wang, G. X., Lotnyk, A., Li, C. & Shen, X. Oxygen filling voids and direct element imaging of metastable ZnSb structures by aberration-corrected scanning transmission electron microscopy. *Scr. Mater.* **157**, 115–119 (2018).
23. Simpson, R. E., Fons, P. J., Kolobov, A. & Kuwahara, M. Tominaga, Crystallization of bi doped Sb<sub>2</sub>Te<sub>3</sub>. *Jpn. J. Appl. Phys.* **48**, 03A062 (2009).
24. Angell, C. A. Formation of glasses from liquids and biopolymers. *Science* **267**, 1924–1935 (1995).
25. Simpson, R. E. et al. Reduction in crystallization time of Sb:Te films through addition of Bi. *Appl. Phys. Lett.* **92**, 141921 (2008).
26. Dou, X. C., Li, G. H. & Lei, H. C. Kinetic versus thermodynamic control over growth process of electrodeposited Bi/BiSb superlattice nanowires. *Nano Lett.* **8**, 1286–1290 (2008).
27. Palisaitis, J., Hsiao, C. L., Hultman, L., Birch, J. & Persson, P. O. Å. Direct observation of spinodal decomposition phenomena in InAlN alloys during in-situ STEM heating. *Sci. Rep.* **7**, 44390 (2017).
28. Bjerg, L., Madsen, G. K. H. & Iversen, B. B. Ab initio calculations of intrinsic point defects in ZnSb. *Chem. Mater.* **24**, 2111–2116 (2012).
29. Wang, G. et al. Investigation on pseudo-binary ZnSb-Sb<sub>2</sub>Te<sub>3</sub> material for phase change memory application. *J. Alloys Compd.* **622**, 341–346 (2015).
30. Eklof, D. et al. Transport properties of the II-V semiconductor ZnSb. *J. Mater. Chem. A* **1**, 1407–1414 (2013).
31. Khang, N. H. D., Ueda, Y. & Hai, P. N. A conductive topological insulator with large spin hall effect for ultralow power spin-orbit torque switching. *Nat. Mater.* **17**, 808–813 (2018).
32. Siegrist, T. et al. Disorder-induced localization in crystalline phase-change materials. *Nat. Mater.* **10**, 202–208 (2011).
33. Volker, H., Jost, P. & Wuttig, M. Low-temperature transport in crystalline Ge<sub>3</sub>Sb<sub>2</sub>Te<sub>4</sub>. *Adv. Funct. Mater.* **25**, 6390–6398 (2015).
34. Jost, P. et al. Disorder-induced localization in crystalline pseudo-binary GeTe-Sb<sub>2</sub>Te<sub>3</sub> alloys between Ge<sub>3</sub>Sb<sub>2</sub>Te<sub>6</sub> and GeTe. *Adv. Funct. Mater.* **25**, 6399–6406 (2015).
35. Fedorov, M. I. et al. New interest in intermetallic compound ZnSb. *J. Electron. Mater.* **43**, 2314–2319 (2014).
36. Murmu, P. P., Chong, S. V., Storey, J., Rubanov, S. & Kennedy, J. Secondary phase induced electric conductivity and improvement in thermoelectric power factor of zinc antimonide films. *Mater. Today Energy* **13**, 249–255 (2019).
37. Liu, W. et al. Studies on Bi<sub>2</sub>Te<sub>3</sub>-Bi<sub>2</sub>Se<sub>3</sub>-Bi<sub>2</sub>S<sub>3</sub> System for mid-temperature thermoelectric energy conversion. *Energy Environ. Sci.* **6**, 552–560 (2013).
38. Xiao, Y. & Zhao, L. D. Charge and phonon transport in PbTe-based thermoelectric materials. *NPG Quantum Mater.* **3**, 55 (2018).
39. Joshi, G. et al. Enhanced Thermoelectric figure-of-merit in nanostructured p-type silicon germanium bulk alloys. *Nano Lett.* **8**, 4670–4674 (2008).
40. Chen, Y. et al. Bendable n-type metallic nanocomposites with large thermoelectric power factor. *Adv. Mater.* **29**, 1604752 (2017).